Precision Engineering 34 (2010) 307–319

Contents lists available at ScienceDirect

Precision Engineering

journal homepage: www.elsevier.com/locate/precision

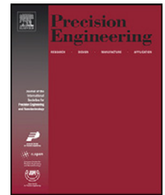

Design and modeling of a six DOFs MEMS-based precision manipulator

D.M. Brouwer[a,b,*], B.R. de Jong[c,1], H.M.J.R. Soemers[a,d,2]

[a] University of Twente, Horst HR W222, Drienerlolaan 5, 7500 AE Enschede, The Netherlands
[b] DEMCON, Zutphenstraat 25, 7575 EJ Oldenzaal, The Netherlands
[c] Philips Applied Technologies, Electronic Packaging & Thin Film, HTC7 3A.035, 5656 AE Eindhoven, The Netherlands
[d] Philips Applied Technologies, Building WDX 2.A.032, High Tech Campus 7, 5856 AE Eindhoven, The Netherlands

ARTICLE INFO

Article history:
Received 25 July 2008
Received in revised form 18 May 2009
Accepted 5 August 2009
Available online 12 August 2009

Keywords:
MEMS
Manipulator
Precision
Exact constraint design
Six degrees-of-freedom
DOFs
Micro-systems technology
MST
Compliant mechanisms
Elastic mechanism
Flexure mechanisms

ABSTRACT

In this paper a design is presented for a precision MEMS-based six degrees-of-freedom (DOFs) manipulator. The purpose of the manipulator is to position a small sample ($10\,\mu m \times 20\,\mu m \times 0.2\,\mu m$) in a transmission electron microscope. A parallel kinematic mechanism with slanted leaf-springs is used to convert the motion of six in-plane electrostatic comb-drives into six DOFs at the end-effector. The manipulator design is based on the principles of exact constraint design, resulting in a high actuation compliance (flexibility) combined with a relatively high suspension stiffness. However, due to fabrication limitations overconstrained design has been applied to increase the stiffness in the out-of-plane direction. The result is a relatively large manipulator stroke of $20\,\mu m$ in all directions combined with a high first vibration mode frequency of 3.8 kHz in relation to the used area of $4.9\,mm \times 5.2\,mm$. The motion of the manipulator is guided by elastic elements to avoid backlash, friction, hysteresis and wear, resulting in nanometer resolution position control. The fabrication of the slanted leaf-springs is based on the deposition of silicon nitride (Si_xN_y) on a silicon pyramid, which in turn is obtained by selective crystal plane etching by potassium hydroxide (KOH). The design has been analyzed and optimized with a multibody program using flexible beam theory. A previously developed flexible beam element has been used for modeling the typical relatively large deflections and the resulting position-dependent behavior of compliant mechanisms in MEMS. The multibody modeling has been verified by FEM modeling. Presently only parts of the manipulator have been fabricated. Therefore, a scaled-up version of the manipulator has been fabricated to obtain experimental data and to verify the design and modeling.

© 2009 Elsevier Inc. All rights reserved.

1. Introduction

In the future, the precision manipulation of small objects will become more and more important for appliances such as (probe-based) data storage, micro-assembly, sample manipulation in microscopes, cell manipulation, nano-indenting, manipulation of optical beam paths by micro-mirrors and manipulation of electron beam paths by phase plates. At the same time, there is a drive towards miniaturized systems. An example can be found in the manipulation of samples in a transmission electron microscope (TEM). The relatively large dimensions of 'conventional' TEM sample manipulators result in typical drawbacks such as thermal drift and compromised dynamics. Especially the requested stability of 0.1 nm/min requires a new manipulator concept. Miniaturization creates the opportunity to fix the manipulator directly to the column which guides the electron beam, isolating external thermal and vibration noise. Secondly miniaturizing the manipulator generally results in enhanced stability because of increased natural frequencies, decreased thermal drift and in small thermal time constants of the manipulator. Potential solutions for miniaturizing can be found in Micro Electro Mechanical Systems (MEMS). MEMS devices comprise micro-sensors, actuators, mechanisms, optics and fluidic systems. They have the ability to integrate several functions in a small package. Precision manipulation in MEMS seems sparse however.

Combining design principles, a mature design philosophy for creating precision machines, and MEMS fabrication, a technology for miniaturization, could lead to micro-systems with deterministic behavior and accurate positioning capability. However, in MEMS design trade-offs need to be made between fabrication complexity and design principle requirements. A micro-mechatronic design of a parallel kinematic six degrees-of-freedom MEMS-based preci-

* Corresponding author at: University of Twente, Mechanical Automation and Mechatronics, IMPACT Research Institute, Horst HR W222, Drienerlolaan 5, 7500 AE Enschede, The Netherlands. Tel.: +31 6 14246303/0541 570720; fax: +31 541 570721.

E-mail addresses: d.m.brouwer@utwente.nl (D.M. Brouwer), boudewijn.de.jong@philips.com (B.R. de Jong), h.m.j.soemers@philips.com (H.M.J.R. Soemers).

[1] Tel.: +31 040 27 48219; fax: +31 040 27 46377.
[2] Tel.: +31 6 53337793; fax: +31 40 2746355.

0141-6359/$ – see front matter © 2009 Elsevier Inc. All rights reserved.
doi:10.1016/j.precisioneng.2009.08.001

sion manipulator is presented. Although presently only parts of the fabrication process have been tested [1], the conceptual manipulator design is verified by measurement data on a scaled-up version. The research, design and fabrication of a multi-DOFs micro-stage will be continued.

2. Requirements

The requirements of the manipulator are based on a next generation TEM sample manipulator. First, the manipulator has to operate in an ultra high vacuum (10^{-8} to 10^{-9} mbar) and should not interfere with the electron beam. The maximum displacement should be enough to examine a sample. A semiconductor sample is typically 20 μm × 10 μm × 0.2 μm. Therefore, the *x*- and *y*-strokes of the manipulator should be about 20 μm. For the focusing of the electron beam, the *z*-stroke should be about 20 μm also. Once an area of interest is found on the sample, the TEM sample manipulator should be able to find this area again with a translational repeatability of about 10 nm. Extremely fine positioning is possible by manipulating the electron beam itself. The MEMS-based manipulator will be used for small correction angles up to several degrees only. The rotational repeatability needs to be better than 0.05°.

Some TEMs can be used in a scanning TEM (STEM) mode, where the beam can be scanned across the sample to form the image. Taking a picture in the STEM mode can take up to half a minute. This fact, combined with the possible image resolution of 0.08 nm, results in an extreme stability requirement of 0.1 nm/min for the sample with respect to the electron beam. This stability should be reached within 10 s after the manipulation of the sample. Because of the high resolution capability of the TEM, sound and the vibrating surroundings cause the TEM column to vibrate, which could lead to blurred images. Therefore, the sample needs to be fixed dynamically stable to the TEM column. Therefore, a next generation manipulator requires a lowest vibration mode frequency of more than 1 kHz. A summary of the main specifications is given in Table 1.

3. Background of multi-DOFs positioning in MEMS

To develop an idea of the state of the art of precision positioning in MEMS, a small survey is presented with respect to existing examples of multi-DOFs devices in MEMS. The MEMS-based manipulators are distinguished with respect to systems for planar positioning, systems for out-of-plane positioning and combinations of both. For positioning repeatability it is important that the mechanism used in a manipulator does not have friction, play or backlash [2–8]. Many solutions for multi-DOFs hinges offering large freedom of movement show play and friction in the hinges [9–12]. This is a large drawback for precision applications and is therefore not regarded. Compliant mechanisms using elastic hinges generally do not suffer from friction, play and backlash and are far more suited to precision manipulation. However, the displacements are limited compared to the size of the mechanism.

Table 1
Specifications for a next generation TEM sample manipulator.

Property	Value
Stroke *x*, *y*, *z*	20 μm
Repeatability *x*, *y*, *z*	10 nm
Rotational stroke (any 2 DOFs)	3°
Rotational repeatability	0.05°
Stability[a]	0.1 nm/min
1st vibration mode frequency	>1 kHz

[a] Value should be reached within 10 s after manipulation.

3.1. In-plane positioning

A 2 DOFs planar manipulation platform is presented by Sarajlic et al. [13]. The platform is actuated by electrostatic comb-drives. The 2 DOFs of the planar manipulator are generated by a series coupling of movements of about 20 μm in both directions. The positioning resolution is limited by the resolution of the amplifier. The system is fabricated by a bulk micro-machining process in single crystal silicon. Etching in the bulk wafer is called bulk micro-machining. In the case of a silicon wafer, it results in single crystal silicon as a structural material. Bulk micro-machining allows high aspect-ratio structures, for example leaf-springs with a thickness of 2 μm and a height of 40 μm. Using comparable fabrication technology, an example of a parallel 3 DOFs planar manipulator has been fabricated by de Jong et al. [14]. The manipulator uses a compliant mechanism of the parallel kinematic type to convert the motion of 3 stationary actuators to 3 DOFs of the platform. The translational strokes are 20 μm and the maximum rotation is 4°. Stepper or inchworm actuators are also found in the micro-domain. Examples of electrostatic parallel plate actuators for clamping and displacement are given by Tas [15] and Patrascu et al. [16] for single DOF displacement and by Sarajlic et al. in [17] for 2 DOFs displacement.

3.2. Out-of-plane positioning

In [18] a 3 DOFs out-of-plane manipulation stage is presented applying three identical linear motors consisting of a slider and a pair of thermal bimorph actuators. The motors are radially positioned around a platform with 120° pitch and push radially inward. The propulsion is based on friction, which is generally a drawback for precision positioning. Another 3 DOFs out-of-plane stage applying the same kinematic principle is presented in [19]. Here electrostatic scratch-drive actuators are applied. A scratch-drive actuator is a kind of stepping electrostatic actuator. For this stage, hinges are used with play instead of hinge flexures. A 3 DOFs out-of-plane stage with compliant hinges made from polydimethylsiloxane (PDMS) is presented in [20]. Out-of-plane actuation is based on a mechanism, built up out of PDMS, transforming the in-plane motion of comb-drives to out-of-plane displacements of a platform.

3.3. Combinations of in- and out-of-plane manipulation

In [21], Sarkar et al. present various multi-DOFs manipulators for inspection inside a TEM or SEM. These are based on compliant mechanisms and driven by thermo-mechanical bimorph actuators made in a surface micro-machining process. Culpepper et al. [22] have designed a symmetric flexure mechanism for six DOFs manipulation called HexFlex. In [23] a MEMS version of this mechanism is presented driven by 12 thermo-mechanical actuators arranged in 6 pairs. The choice for this type of thermo-mechanical actuators allows relatively simple fabrication. However, the system is over-actuated and the thermal heat influences the position stability of a TEM system. Ando [24] has presented a compliant mechanism 3 DOFs stage with strokes of 1.0, 0.13 and 0.4 μm in the *x*-, *y*- and *z*-direction. Inclined leaf-springs are used fabricated by focused ion beam milling. Liu et al. [25] reported a 3 DOFs manipulator with strokes of 25, 25 and 3.5 μm in the *x*-, *y*- and *z*-direction. The positioning repeatability open-loop is better than 17.3 nm along all three axes.

3.4. Assembly of MEMS devices

The literature describes many examples of wafer-bonding of MEMS devices. A very nice example of assembly by wafer-bonding

is a micro-turbine presented in [26], where a total of five wafers are stacked on top of each other. Another example where four wafers are stacked is given in [27] for a 2 DOFs tilt mirror with buried actuators. An assembled magnetic induction machine is presented in [28] and [29]. Here, a rotor structure is assembled on top of a molded coil structure. Tsui et al. [30] have developed modular construction elements made from silicon that are assembled with the aid of compliant connectors and sockets. This assembly requires a macroscopic external precision manipulator system. Using this technique, a micro-SEM is developed [31].

3.5. Conclusion regarding existing research

None of the literature studied in the survey described above reports characterization with respect to stability and resolution. As mentioned before, this is typical of literature on MEMS systems and understandable, since obtaining the required measurement data is very challenging. Designing for precision is clearly a rather new discipline within the field of MEMS. However, there is no fundamental reason why positioning in MEMS cannot be accomplished on a nanometer level. In the macro-scale world, precision machines are usually designed by using precision engineering. A design synthesis of precision engineering, a proven design philosophy for creating precision machines, and MEMS, a technology for miniaturization, could lead to precision micro-scale manipulators.

4. MEMS-based mechatronic system design

There are some important differences between a mechatronic design in MEMS and in the macro-scale world. In MEMS the influence of the fabrication technology on the design is large, the fabrication technology is often based on planar processes, the actuator choice influences the used fabrication technology and is therefore great, and sensing is relatively inaccurate in relation to the range of motion.

Roughly, MEMS fabrication can be subdivided into ‘bulk micro-machining’ based processes [32], and ‘surface micro-machining’ based processes. Surface micro-machining is basically deposition and removal of relatively thin layers of material on a wafer. In bulk micro-machining processes the wafer itself is etched resulting in high (out-of-wafer-plane) structures. High aspect-ratio structures, such as leaf-springs of 35–40 μm high and 2 μm thick, can be made by Deep Reactive Ion Etching (DRIE). High leaf-springs are necessary for increasing the out-of-wafer-plane stiffness of the relatively large MEMS devices. Electrical wiring in bulk micro-machined devices can be done by so called trench isolation [13] or using SOI technology. A wall of insulation material divides the silicon resulting in isolated electrical parts.

The design principles which are especially relevant for the manipulator design are determinism, exact constraint design and symmetry [3]. Exact constraint design means a design has exactly the required amount of compliant (ideally free) and stiff (ideally constrained) degrees-of-freedom necessary to create a specified motion. The exact constraint design makes the actuation modes compliant, reducing the energy necessary for actuation. At the same time the exact constraint design makes the suspension modes relatively stiff, leading to high suspension mode frequencies, reduced sensitivity for disturbances and a robust overall design. In addition, a design which is based on a fully compliant mechanism avoids backlash, friction, wear and minimizes hysteresis, resulting in highly deterministic behavior. Symmetry often improves the dynamic behavior by increasing disturbing vibration mode frequencies and by making mode shapes less disturbing.

The manipulator design is based on the design principles, ‘determinism’ by using a fully compliant mechanism, and ‘exact constraint design’ in combination with mainly bulk micro-machining processes.

4.1. Six DOFs motion

Six DOFs positioning requires both in-plane and out-of-plane motion. Basically the two options for six DOFs motion generation are using a combination of in-plane and out-of-plane actuators in one system, or using one type of actuator and a mechanism to convert in-plane to out-of-plane motion or vice versa. Usually the technology to fabricate in-plane actuators differs from the technology to fabricate out-of-plane actuators. Therefore, a combination between the two is a rarity. Although it is easier to fabricate six actuators of the same type than three in-plane and three out-of-plane actuators, the mechanism needed to convert motion usually also requires special additional process steps. The combination of a motion converting mechanism with one type of actuator has been used in the manipulator design.

4.2. Actuation principle in MEMS

A summary of the overview regarding actuation principles in MEMS presented in [33] is given. MEMS-based magnetic actuators have a low energy density. Piezo (PZT) actuators are difficult to integrate in MEMS technology or need assembly. Thermal actuators can have an energy density comparable to electrostatic actuators. In general, thermal actuators lack thermal stability, causing position uncertainty at nano-manipulation. Regarding the necessary stroke and force of the manipulator a lateral comb-drive electrostatic actuator would suffice. This type of actuator integrates well into bulk micro-machining. Six electrostatic comb-drives will be used for actuation. The problem of the interaction of the electron beam with electrostatic actuators can be overcome by either blocking the actuators with a clamp or by shielding. The typical electrostatic force per finger pair at 60 V is 0.5 μN.

In general the actuators used in MEMS exhibit low work density compared to the energy storage in elastic elements. Consequently the actuators in MEMS are relatively large and the elastic elements are generally long and slender.

4.3. Serial versus parallel kinematic mechanism

A distinction can be made between serial and parallel type of mechanisms. A serial mechanism consists of one kinematic chain of links and joints between the end-effector and base to enable all DOFs. A parallel mechanism has several kinematic chains between the end-effector and base. In MEMS a parallel mechanism can be used to convert motion from in-plane to out-of-plane. The high vibration mode frequencies in this case are convenient in the TEM application for a good mechanical coupling between the TEM column and the sample. A large advantage of a parallel set-up, especially in MEMS, is that the actuators are stationary. This makes routing of the electrical connections, generally difficult in MEMS, to the actuators (and sensors) easy.

4.4. Position control

Two specifications with respect to positioning need to be distinguished: the positional repeatability and the stability. The repeatability specified at 10 nm is the uncertainty at which the manipulator can reproduce a position each time. The stability of 0.1 nm specifies how well the position is kept constant relative to the electron beam over a certain amount of time, in this case 1 min.

Precision macro-systems often rely on feedback for accurate position information. Measuring on the micro-scale is less trivial. With respect to the repeatability the external disturbance forces

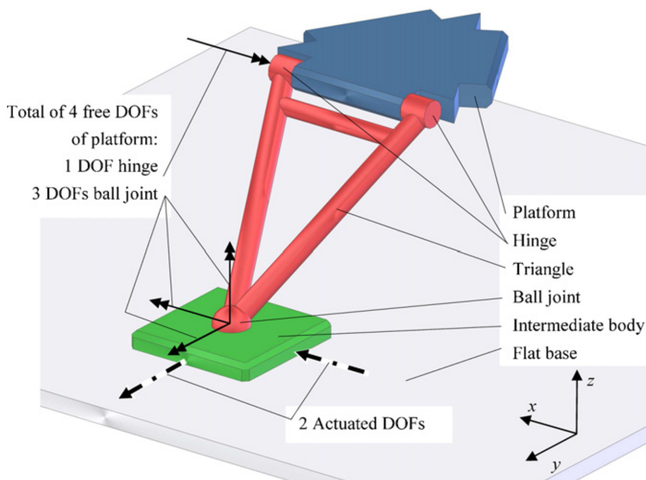

Fig. 1. One of the three legs of the manipulator with the platform.

loading the manipulator are small. In this case a monolithic and single crystal mechanical structure in MEMS leads to a highly repeatable mechanism. Therefore, using only feed-forward control can result in excellent positional repeatability. The stability of the system will rely on passive mechanical stability. There are several reasons why the passive stability can be enhanced by unpowered blocking of the manipulator. A first reason is because the cross-talk between the electron beam of the TEM and electric or magnetic fields from the actuators of the manipulator affects the stability of the electron beam and the manipulator. Clamping (of course without generating electric or magnetic fields) decreases this cross-talk. A second reason is, the manipulator can be switched between compliant actuation modes for positioning, and high frequent vibration modes during imaging. A clamping mechanism has been developed for this purpose [34]. In the final design a mechanical clamp with a locking device is integrated.

5. The kinematic concept

The manipulator, which is schematically shown in Fig. 2, has a *flat base* over which 3 *intermediate bodies* can move. Each *intermediate body* is actuated in 2 translational DOFs (x and y in Fig. 1) and constrained in the other 4 DOFs (z, Rx, Ry and Rz). The *ball joint* connecting the *intermediate body* with the *triangle* releases 3 DOFs. Therefore the *triangle* has 2 actuated, 3 free and 1 constrained DOFs. The *hinge*, also called revolute joint, releases another DOF. Therefore, the *platform* has 2 actuated and 4 free DOFs by one leg as shown in Fig. 1. Table 2 summarizes the DOFs per leg.

The combination of 3 times 2 DOFs actuated per leg results in the platform having six DOFs actuated. Each of the individual DOFs of the platform is shown with the corresponding intermediate body xy-translations in Fig. 2.

The kinematic concept as implemented in the MEMS-based manipulator, shown in Fig. 3, is almost equivalent to the kinematic concept shown in Fig. 1. The suspension of the actuator is regarded as constraining five DOFs and leaving compliant only the actuation direction. Each leaf-spring is regarded as constraining three DOFs. Three DOFs of the intermediate body, shown in Fig. 4, are stiff (ideally constrained by the Si-leaf-springs). Two DOFs of the intermediate body are actuated by electrostatic comb-drives [35]. The two Si-leaf-springs, which are connected at the intermediate body, leave one DOF compliant, the rotation around their intersection. The slanted leaf-spring releases three DOFs, which can be regarded as three rotational DOFs, as shown in Fig. 5. The three compliant DOFs near the intermediate body can be regarded as a ball joint, equivalent to the ball joint in Fig. 1. Although these three rotational compliant DOFs are not orthogonal, they do act as an elastic ball joint, because their vector span a 3D space and intersect close to each other. The compliant DOF near the platform can be regarded as the hinge equivalent of Fig. 1. The combination of three times two DOFs actuated per leg results in the platform having six DOFs actuated (Fig. 3).

Each intermediate body is constrained twice in the z-direction by the connecting Si-leaf-springs, resulting in an overconstrained design. However the z-stiffness of the Si-leaf-springs is limited (which will be shown in the Section 8.1) because of dimensions resulting from fabrication. Therefore the overconstrained design effectively helps to increase the z-stiffness. The overconstrained design will not lead to large stresses and therefore changed system behavior [40] because the mechanism is fabricated out of one piece of low stress material and the processing does not lead to stress in the mechanism. Each electrostatic actuator is suspended by four folded flexures [35], which also results in an overconstrained design. However, the gain in stiffness in the z-direction due to the overconstrained is more essential. In fact each folded flexure itself is overconstrained and at the same time the intermediate body of the folded flexure (Fig. 4) is also underconstrained. The underconstrained internal vibration mode frequency of the folded flexure is high and is therefore not significantly disturbing the system. However, the suspension stiffness of the folded flexure decreases due to the underconstrained internal mode at large deflections [1], which could lead to electrostatic actuator instability [35]. The stiffness decrease due to deflection in the case of the manipulator design is limited because the deflection is limited.

Important for the design is that overconstraints have only been applied to increase the z-stiffness of the intermediate body. The overconstrained design does not lead to large stresses and the resulting changed system behavior because of the limited height to length ratio of the leaf-springs. The compliant actuation direction does not suffer from the overconstrained design. Exact constraint design has necessarily been applied at the slanted leaf-springs, because the slanted leaf-spring dimensions would cause large internal stress due to stress resulting from processing or deformation due to maneuvering in case of an overconstrained design. In the case of a design containing underconstraints unacceptable low frequency vibration modes would be encountered. This is not the case with the manipulator design.

To give an impression of the dimensions: the overall size is 4.9 mm × 5.2 mm. The platform is elevated 460 μm above the comb-drives, folded flexures and Si-leaf-springs. Because of anisotropic etching along crystal planes of the silicon (used for obtaining the slanted leaf-springs), the 120° rotational symmetry as shown in Fig. 2 is not maintained in the silicon MEMS version of the manipulator.

Table 2
The DOFs of the rigid bodies of 1 leg of the manipulator.

	Free	Actuated	Constrained	
Intermediate body	0	2	7	Ball joint releases 3 DOFs
Triangle	3	2	1	
Platform	4	2	0	Hinge releases 1 DOF

6. Basic steps of the fabrication process design

In this section the fabrication concept is presented. Presently only parts of the manipulator have been fabricated. The entire fabrication concept of the manipulator is described in [1]. Five lithographic mask transfer steps are used in the total of 126 pro-

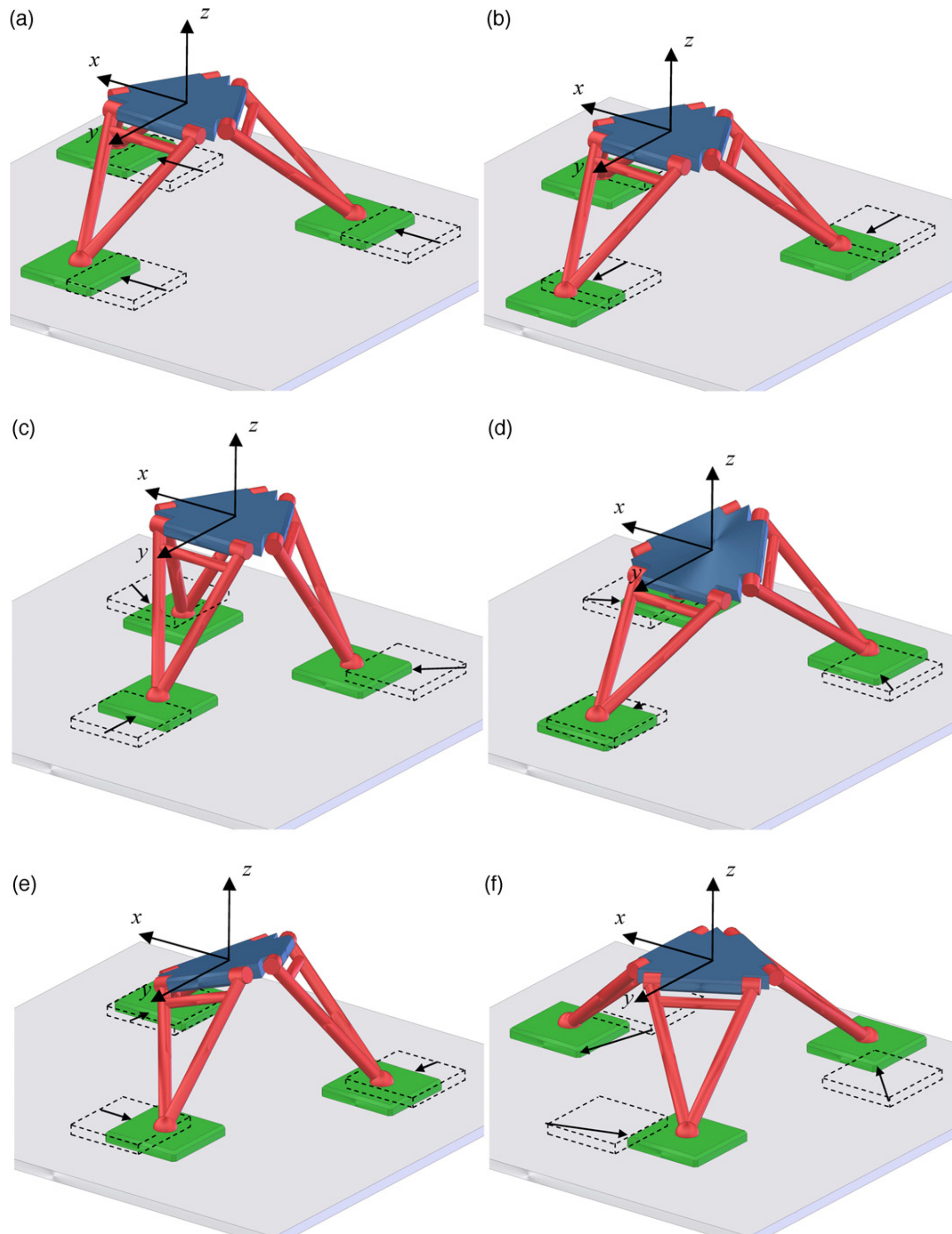

Fig. 2. Each of the independent six DOFs of the platform are created by combinations of planar *xy*-displacements of the three intermediate bodies.

cess steps. The steps are explained in [1]. The concept is based on etching a 460 μm high pyramid, shown in Fig. 6, in a 500 μm ⟨100⟩ thick Si-wafer. A pyramid with flat sides can be etched by potassium hydroxide (KOH) using ⟨100⟩ compensation structures [36]. KOH etches silicon along ⟨111⟩ crystal planes. On three of the flat pyramid sides slanted leaf-springs of silicon nitride (Si_xN_y) are deposited as shown in Fig. 7. The shape of the slanted leaf-springs is structured by evaporation of aluminum through a shadow mask and subsequently etching the leaf-springs. In a next step the pyramid is etched away by reactive ion etching leaving the slanted leaf-springs. An alternative route for fabricating the slanted leaf-springs is to structure and release the silicon nitride slanted leaf-springs by using focused ion beam milling. The comb-drives are etched by DRIE. The electrical wiring is laid out by using trench isolation technology [13].

Top figure show a cross-section of the manipulator after KOH etching. Bottom figure shows the cross-section of the manipulator after the total processing.

7. Dimensioning the manipulator

Many dimensions of the manipulator are determined by the process steps used. The most important dimensions are the ones concerning the elastic elements: the folded flexures, the slanted leaf-springs and the Si-leaf-springs.

7.1. The folded flexures

The design of the comb-drive suspension integrated in the first design of the manipulator is kept relatively conservative, so as not

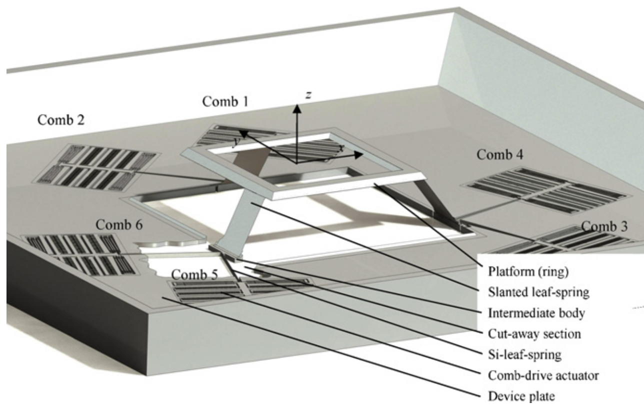

Fig. 3. The MEMS-based six DOFs manipulator design. For viewing purposes a section has been cut away. Overall dimensions are 4.9 mm × 5.2 mm × 0.5 mm.

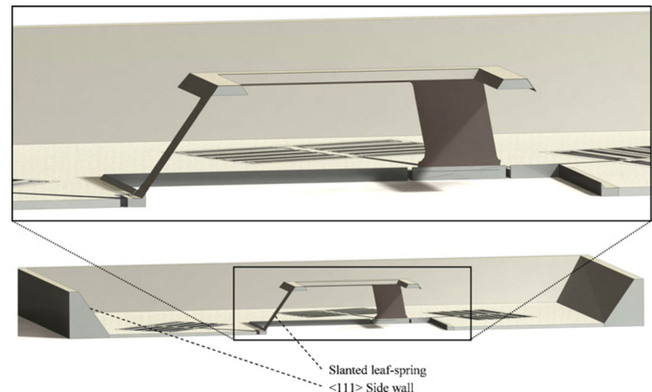

Fig. 6. Cross-section of the six DOFs MEMS-based precision manipulator showing the slanted leaf-springs. The ⟨111⟩ crystal plane orientation obtained by KOH etching is visible.

to accumulate risk. Therefore 4 reinforced folded flexures (Fig. 4) suspend one comb-drive. The comb-drives actuate in one direction only to keep the number of electrical connections low. However, if large strokes are necessary, comb-drives actuating in two directions are preferred. The leaf-spring thickness can be set at 2 μm. However, 3 μm is used to make the mechanism more robust for processing. The reinforcement is 8 μm thick. The leaf-spring height is 35 μm and is determined by trench isolation technology as explained by Sarajlic et al. [13]. The length is a trade-off between the amount of comb-drive energy stored in the leaf-springs and the amount of space needed for the flexures. The length is set at 406 μm.

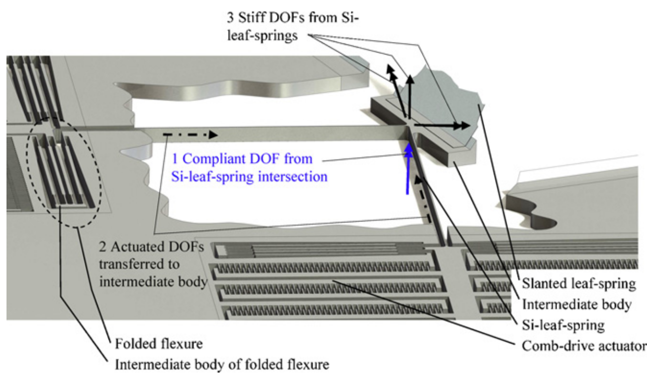

Fig. 4. Three of the three DOFs of the intermediate body are stiff (ideally constrained by the Si-leaf-springs). Two DOFs of the intermediate body are actuated and one DOF is compliant (ideally released).

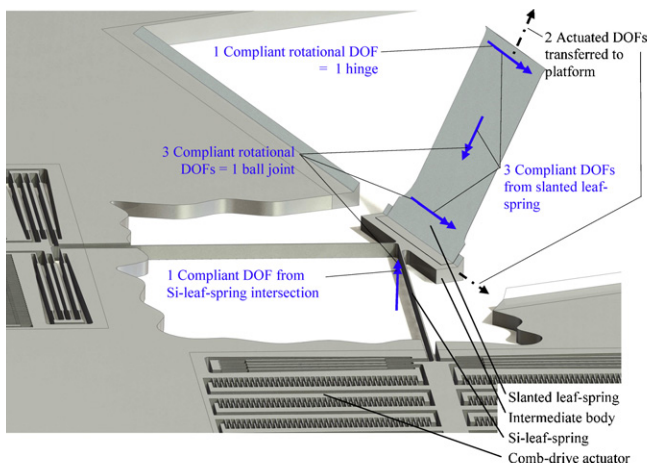

Fig. 5. The six DOFs (2 actuated and 4 compliant) of the platform defined by 1 leg. The slanted leaf-spring releases 3 DOFs. The intersection of the Si-leaf-springs releases 1 DOF. The 3 compliant DOFs near the intermediate body can be regarded as a ball joint, equivalent to the ball joint in Fig. 1. The compliant DOF near the platform can be regarded as the hinge equivalent of Fig. 1.

7.2. The slanted leaf-springs

The slanted leaf-springs create a 54.7° angle with the device plate (Fig. 6) resulting from KOH etching in single crystal silicon. The 54.7° angle in combination with the thickness of the wafer minus the thicknesses of the platform and the device plate results in a 403 μm length. The thickness of the slanted leaf-springs is determined by the low pressure chemical vapor deposition (LPCVD) of Si_xN_y which is generally between 0.3 and 2.5 μm. To keep the stress during processing low, the thickness is kept relatively small at 0.7 μm. The width of the leaf-spring is set at 300 μm. This is relatively large so as to ensure increased robustness against buckling.

7.3. The Si-leaf-springs

The height of the Si-leaf-springs is determined by the thickness of the device plate. The device plate thickness is determined by the maximum height for trench isolation, which is about 35–40 μm. The thickness of the Si-leaf-spring can be as small as 2 μm, limited by the aspect ratio of DRIE. However, 3 μm is used to make the

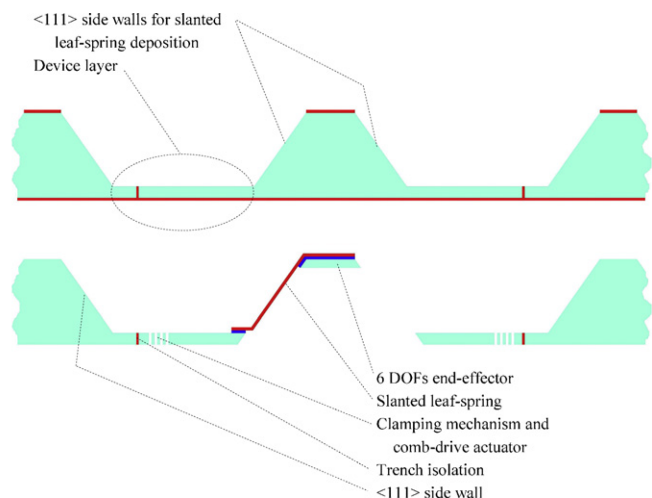

Fig. 7. Brief overview of the fabrication of the six DOFs MEMS-based precision manipulator.

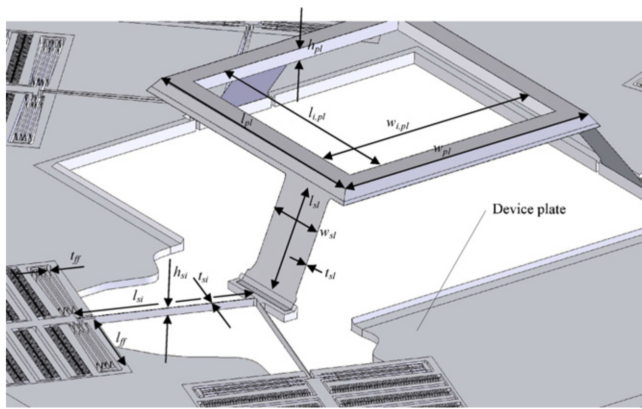

Fig. 8. The dimensions of the manipulator.

mechanism more robust for processing. The length of the Si-leaf-springs needs to be long for a large actuation compliance, which in turn helps to reduce the size of the actuators. If the Si-leaf-spring length is set at 800 μm the folded flexures of the actuator suspension, which require length for compliance too, fit well with the occupied space of the comb-drive.

The dimensions shown in Fig. 8 are listed in Table 3.

8. Overview of the most important dimensions

8.1. Modeling the manipulator

Based on dimensions of the elastic elements (the folded flexures, the slanted leaf-springs and the Si-leaf-springs) the manipulator is modeled to obtain the dimensions of the actuators by calculating the displacement and force output of the actuators. Modeling is also used to obtain the first vibration mode frequencies as a function of the position of the platform and the corresponding vibration mode shapes. Furthermore the stress level in the flexures is calculated, the buckling force on the platform and the thermal stability is investigated.

For design optimization a multibody software program called SPACAR has been used. The program uses the finite beam element described by Meijaard [37] as a basis. To model leaf-springs accurately the influence of constrained warping [38] at the ends of a beam is approximately included by modifying the torsion constant for the elements adjacent to these ends. It is as if the length of the beam is reduced for a beam with wide rectangular cross-section. Shear correction factors are applied according to Cowper [39]. The approach has proven to be accurate for relatively large deflections [1] which are typical for MEMS design. Meijaard [40] even proves that the stress induced by an overconstrained design, which leads to decreased vibration mode frequencies and eventually to bifurcation, can be calculated accurately using the beam model. The approach considerably reduces the number of elements, which makes the analysis fast and effective. The manipulator is modeled by using three beam elements for each leaf-spring. Each beam element in SPACAR has six possible deformation modes. The six possible deformation modes of one beam element are one longitudinal mode, one torsional mode and four bending modes. The varying Young's modulus and Poisson's ratio for different directions in single crystal silicon has been taken into account. The manipulator platform, the intermediate bodies and the comb-drive shuttles have been considered rigid in the SPACAR model.

8.2. Linearized system model of the manipulator

Although SPACAR models the manipulator in any position and orientation taking into account non-linearities, linearized geometrical transfer functions and the stiffness matrices will be derived to physically understand the motion of the platform due to actuation forces, or external forces on the platform. Therefore three 6 × 6 stiffness matrices and a 6 × 6 linear geometric transfer matrix will be derived. Modal analysis is performed by both SPACAR and a finite element method. All matrices have the standard Si dimensions of m, N and radian.

The displacement matrices of the platform $\underline{X}_{pl}$, the actuators $\underline{X}_{act}$, and the force matrices of the platform $\underline{F}_{pl}$ and the actuators $\underline{F}_{act}$ are defined by:

$$\underline{X}_{pl}=\begin{bmatrix}x_{pl}\\y_{pl}\\z_{pl}\\rx_{pl}\\ry_{pl}\\rz_{pl}\end{bmatrix};\quad \underline{X}_{act}=\begin{bmatrix}x_{act\,1}\\x_{act\,2}\\x_{act\,3}\\x_{act\,4}\\x_{act\,5}\\x_{act\,6}\end{bmatrix};\quad \underline{F}_{pl}=\begin{bmatrix}F_{x,pl}\\F_{y,pl}\\F_{z,pl}\\M_{x,pl}\\M_{y,pl}\\M_{z,pl}\end{bmatrix};\quad \underline{F}_{act}=\begin{bmatrix}F_{act\,1}\\F_{act\,2}\\F_{act\,3}\\F_{act\,4}\\F_{act\,5}\\F_{act\,6}\end{bmatrix} \quad (1)$$

Eq. (1) in combination with Fig. 9 shows the definition of the displacement and force matrices. The displacement of the nodes in between the actuators and the platform are represented by matrix

Table 3
The most important dimensions of the manipulator design.

Symbol	Size	Flexure geometry	Dimension constrained by
l_{pl}	1.32 mm	Platform length	Min. length constrained by KOH compensation mask
w_{pl}	1.32 mm	Platform width	Min. width constrained by KOH compensation mask
$l_{i,pl}$	1.12 mm	Inner platform length	Free to choose
$w_{i,pl}$	1.12 mm	Inner platform width	Free to choose
h_{pl}	50 μm	Platform height	Free to choose, needs height for bending stiffness
l_{sl}	403 μm	Slanted leaf-spring length	Defined by wafer thickness, KOH etch angle, platform thickness and the device plate thickness (h_{si})
w_{sl}	300 μm	Slanted leaf-spring width	Free to choose, chosen wide w.r.t. buckling
t_{sl}	0.7 μm	Slanted leaf-spring thickness	Between 0.3 and 2.5 Si_xN_y layer thickness
l_{si}	800 μm	Silicon leaf-spring length	Free to choose, chosen long for actuation compliance
h_{si}	35 μm	Silicon leaf-spring height	Max. height determined by refilling of trench
t_{si}	3 μm	Si-leaf-spring thickness	Thickness greater than 2 μm
l_{ff}	406 μm	Folded flexure length	Free to choose, trade-off between space and actuation compliance
t_{ff}	3 μm	Folded flexure thickness	Thickness greater than 2 μm
t_r	8 μm	Reinforcement thickness	Free, thickened for process robustness
l_f	28 μm	Comb finger length	Free, based on actuator displacement
g_f	3 μm	Comb finger gap	Greater than 2 μm

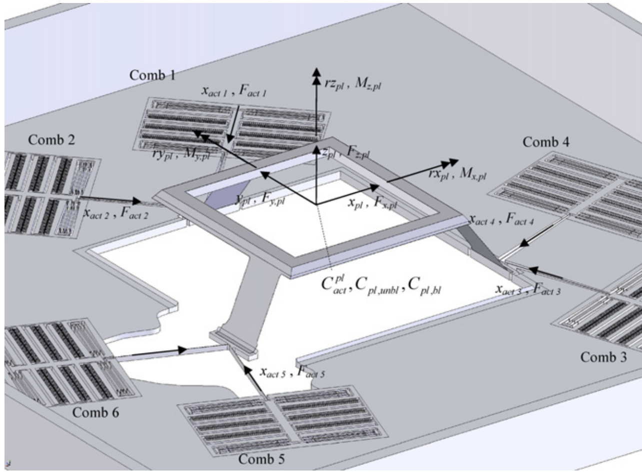

Fig. 9. Definition of the six DOFs platform displacements $\underline{X}_{pl}$, platform forces $\underline{F}_{pl}$, actuator displacements $\underline{X}_{act}$ and actuator forces $\underline{F}_{act}$.

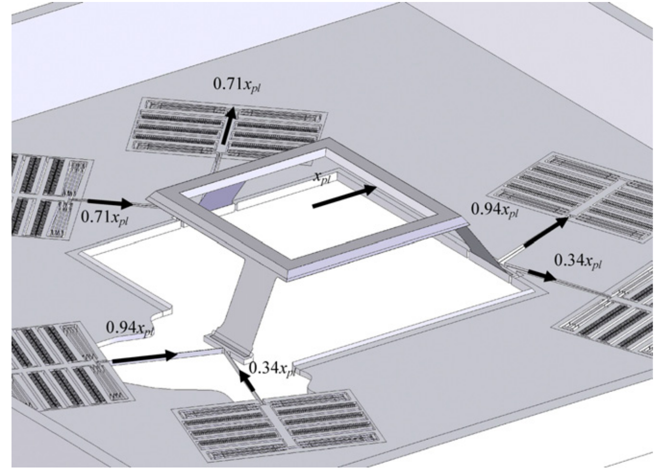

Fig. 10. Example of an in-plane motion in the x-direction x_{pl} of the platform. The relative displacement of each of the actuators is given.

$\underline{X}_r$, with the dual external forces $\underline{F}_r$. In the SPACAR model used, these matrices have a dimension 184×1. The total static linear system model of the total manipulator is given by:

$$\begin{bmatrix} \underline{F}_{act} \\ \underline{F}_{pl} \\ \underline{F}_r \end{bmatrix} = \begin{bmatrix} C_{11} & C_{12} & C_{13} \\ C_{12}^T & C_{22} & C_{23} \\ C_{13}^T & C_{23}^T & C_{33} \end{bmatrix} \cdot \begin{bmatrix} \underline{X}_{act} \\ \underline{X}_{pl} \\ \underline{X}_r \end{bmatrix} \tag{2}$$

and

$$\begin{bmatrix} \underline{X}_{act} \\ \underline{X}_{pl} \\ \underline{X}_r \end{bmatrix} = \begin{bmatrix} S_{11} & S_{12} & S_{13} \\ S_{12}^T & S_{22} & S_{23} \\ S_{13}^T & S_{23}^T & S_{33} \end{bmatrix} \cdot \begin{bmatrix} \underline{F}_{act} \\ \underline{F}_{pl} \\ \underline{F}_r \end{bmatrix} \tag{3}$$

8.3. *Geometric transfer function and actuation stiffness matrix* $\underline{F}_{pl} = \underline{0}; \quad \underline{F}_r = \underline{0}$

In this section a 6×6 linear geometric transfer matrix T will be derived to map the actuator displacements, due to actuator forces, to the platform displacements. In addition a 6×6 stiffness matrix to model the stiffnesses, experienced by the 6 actuators, C_{act}, will be derived. T and C_{act} are valid if the forces acting on the system are solely the actuation forces: $\underline{F}_{pl} = \underline{0}; \quad \underline{F}_r = \underline{0}$. In this case only certain parts of Eq. (3) are of interest:

$$\begin{bmatrix} \underline{X}_{act} \\ \underline{X}_{pl} \\ \underline{X}_r \end{bmatrix} = \begin{bmatrix} S_{11} & \cdot & \cdot \\ {S_{12}}^T & \cdot & \cdot \\ {S_{13}}^T & \cdot & \cdot \end{bmatrix} \cdot \begin{bmatrix} \underline{F}_{act} \\ \underline{0} \\ \underline{0} \end{bmatrix} \tag{4}$$

The external forces on the actuators $\underline{F}_{act}$ result in a coupling of the displacement of the platform $\underline{X}_{pl}$ to the displacement of the actuators $\underline{X}_{act}$:

$$\begin{aligned} \underline{X}_{act} &= T \cdot \underline{X}_{pl} \\ T &= S_{11} \cdot \left({S_{12}}^T\right)^{-1} \end{aligned} \quad \Leftarrow \underline{F}_{pl} = \underline{0}; \underline{F}_r = \underline{0} \tag{5}$$

Matrix transformation of Eq. (5) results in the transformation of the dual forces, the actuator forces and the platform forces, in which $\underline{F}_{pl,img}$ are the imaginary forces resulting from $\underline{F}_{act}$, acting on the platform:

$$T^T \cdot \underline{F}_{act} = \underline{F}_{pl,img} \quad \Leftarrow \underline{F}_{pl} = \underline{0}; \underline{F}_r = \underline{0} \tag{6}$$

The actuator stiffness matrix C_{act} can be defined as follows:

$$\begin{aligned} \underline{F}_{act} &= C_{act} \cdot \underline{X}_{act} \\ C_{act} &= {S_{11}}^{-1} \end{aligned} \quad \Leftarrow \underline{F}_{pl} = \underline{0}; \underline{F}_r = \underline{0} \tag{7}$$

The stiffness matrix C_{act} can be transformed to a stiffness matrix C_{act}^{pl}, which is the stiffness matrix geometrically located in the center of the platform as shown in Fig. 9. At a later stage this stiffness matrix will be used to compare with the unblocked platform stiffness matrix.

$$C_{act}^{pl} = T^T \cdot C_{act} \cdot T = S_{12}^{-1} \cdot S_{11}^T \cdot \left(S_{12}^T\right)^{-1} \quad \Leftarrow \underline{F}_{pl} = \underline{0}; \underline{F}_r = \underline{0} \tag{8}$$

The actuator forces displacing the platform can be written as:

$$\underline{F}_{act} = (T^T)^{-1} \cdot C_{act}^{pl} \cdot \underline{X}_{pl} = \left(S_{12}^T\right)^{-1} \cdot \underline{X}_{pl} \quad \Leftarrow \underline{F}_{pl} = \underline{0}; \underline{F}_r = \underline{0} \tag{9}$$

The linearized geometric transfer can be determined numerically. The geometric transfer matrix T linearized around its undeflected state is given by:

$$\begin{bmatrix} x_{act\,1} \\ x_{act\,2} \\ x_{act\,3} \\ x_{act\,4} \\ x_{act\,5} \\ x_{act\,6} \end{bmatrix} = \begin{bmatrix} -0.706 & -0.692 & 0.963 & 0.000710 & 0.000341 & 0.000736 \\ 0.706 & -0.692 & 0.963 & 0.000710 & -0.000341 & -0.000736 \\ -0.341 & 0.927 & 0.482 & 0.000173 & -0.000338 & 0.000769 \\ -0.936 & -0.370 & 1.323 & -0.000930 & -0.000926 & -0.000924 \\ 0.341 & 0.927 & 0.482 & 0.000173 & 0.000338 & -0.000769 \\ 0.936 & -0.370 & 1.323 & -0.000930 & 0.000926 & 0.000924 \end{bmatrix} \begin{bmatrix} x_{pl} \\ y_{pl} \\ z_{pl} \\ rx_{pl} \\ ry_{pl} \\ rz_{pl} \end{bmatrix} \tag{10}$$

For small displacements the actuators displacement can now be related to the displacements of the platform. For example, the linearized actuator displacement for each comb-drive for an x_{pl} platform displacement, is shown in Fig. 10. It is equal to the first column of T of Eq. (10).

The stiffness matrix C_{act}^{pl} is given by:

$$C_{act}^{pl} = \begin{bmatrix} 41.2 & 0 & 0 & 0 & 0.0185 & 0.0003 \\ 0 & 40.7 & -21.1 & -0.00959 & 0 & 0 \\ 0 & -21.1 & 82.8 & -0.0103 & 0 & 0 \\ 0 & -0.00959 & -0.0103 & 0.0000412 & 0 & 0 \\ 0.0185 & 0 & 0 & 0 & 0.0000309 & 0.0000241 \\ 0.0003 & 0 & 0 & 0 & 0.0000241 & 0.0000560 \end{bmatrix} \tag{11}$$

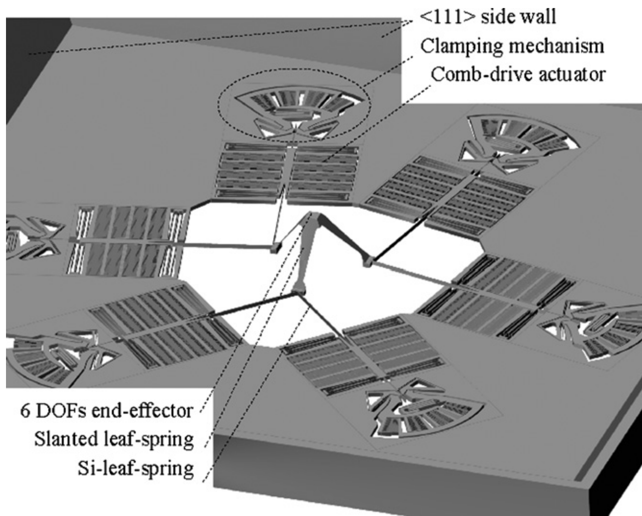

Fig. 11. The six DOFs MEMS-based precision manipulator with clamping mechanisms.

The direct equation to determine the actuator forces that result in a platform displacement is given by:

$$\begin{bmatrix} F_{act\,1} \\ F_{act\,2} \\ F_{act\,3} \\ F_{act\,4} \\ F_{act\,5} \\ F_{act\,6} \end{bmatrix} = \begin{bmatrix} -10.70 & -10.24 & 14.77 & 0.01126 & 0.00607 & 0.01142 \\ 10.70 & -10.24 & 14.77 & 0.01126 & -0.00607 & -0.01142 \\ -4.39 & 12.31 & 6.83 & 0.00268 & -0.00525 & 0.01038 \\ -12.35 & -5.02 & 18.07 & -0.01306 & -0.01255 & -0.01256 \\ 4.39 & 12.31 & 6.83 & 0.00268 & 0.00525 & -0.01038 \\ 12.35 & -5.02 & 18.07 & -0.01306 & 0.01255 & 0.01256 \end{bmatrix} \begin{bmatrix} x_{pl} \\ y_{pl} \\ z_{pl} \\ rx_{pl} \\ ry_{pl} \\ rz_{pl} \end{bmatrix} \quad (12)$$

8.4. Actuation force and stroke

An estimation of the actuation force and stroke can be made using SPACAR. To reach the specified translations in all directions and small correctional rotations at the same time, the actuators need displacements of about 50 μm in two directions. This actuator stroke is rather large, which is due to the parallel kinematic manipulator set-up. The "individual platform displacements" are about 5 times larger than the "combined platform displacements", with the same actuator strokes. Therefore, in a first fabrication design of the manipulator the displacements of the comb-drives are limited to reduce risk. At a stroke of 20 μm the most demanding actuator needs to deliver about 275 μN. For MEMS this calculated force is rather large and requires a voltage of 105 V and 240 finger pairs [35].

In comparison to slanted and Si-leaf-springs, the folded flexures are relatively stiff in the actuation direction consuming at least 80%, depending on the platform position, of the actuator force. This is partly a consequence of the necessity to have a high z-stiffness of the platform and the large force leverage by the Si-leaf-springs from the platform to the folded flexures.

8.5. Platform stiffness blocked and unblocked

For transmission electron microscope (TEM) sample manipulation, the intended application of the manipulator presented in this paper, all six actuators of the manipulator should be fixed without a magnetic or electric field. A mechanical clamping mechanism with a locking device can be integrated in the manipulator for that purpose [34]. Clamping also prevents the six low frequency vibration modes resulting from the compliance in the actuation direction of the folded flexures. Each of the six actuators of the six DOFs manipulator, can be equipped with a clamping mechanism, as shown in Fig. 11.

In this section two stiffness matrices, $C_{pl,unbl}$ and $C_{pl,bl}$, which couple the forces loaded onto the platform to the displacements of the platform, will be derived. $C_{pl,bl}$, is a 6×6 stiffness matrix to model the six DOFs stiffness of the platform for the situation that the actuators are blocked by the clamping mechanisms. $C_{pl,unbl}$, is a 6×6 stiffness matrix to model the six DOFs stiffness of the platform for the unblocked actuator situation.

The unblocked stiffness of the platform couples the forces loaded onto the platform to the displacements of the platform, if there are no other external forces loaded on the manipulator, and at an initially undeflected manipulator state. In this case only certain parts of Eq. (3) are of interest:

$$\begin{bmatrix} \underset{\sim}{X}_{act} \\ \underset{\sim}{X}_{pl} \\ \underset{\sim}{X}_{r} \end{bmatrix} = \begin{bmatrix} \cdot & S_{12} & \cdot \\ \cdot & S_{22} & \cdot \\ \cdot & S_{23}^{T} & \cdot \end{bmatrix} \cdot \begin{bmatrix} \underset{\sim}{0} \\ \underset{\sim}{F}_{pl} \\ \underset{\sim}{0} \end{bmatrix} \quad (13)$$

then

$$\underset{\sim}{F}_{pl} = C_{pl,unbl} \cdot \underset{\sim}{X}_{pl} = S_{22}^{-1} \cdot \underset{\sim}{X}_{pl} \quad \Leftarrow \underset{\sim}{F}_{act} = \underset{\sim}{0}; \underset{\sim}{F}_{r} = \underset{\sim}{0} \quad (14)$$

Although the stiffness matrix C_{act}^{pl}, used to couple the actuator forces to the platform displacement, is located at the same place as $C_{pl,unbl}$, it is fundamentally different. This can be seen by comparing Eqs. (8) and (14). $C_{pl,unbl}$ is the stiffness experienced by a force acting on the platform, while C_{act}^{pl} is the stiffness of the platform as experienced by the actuators.

The values of $C_{pl,unbl}$ are derived numerically from SPACAR and are linearized around the undeflected state. Eqs. (14) and (15) give the equation for the unblocked manipulator:

$$C_{pl,unbl} = \begin{bmatrix} 24.9 & 0 & 0 & 0 & 0.00171 & -0.00912 \\ 0 & 31.7 & -8.4 & 0.00864 & 0 & 0 \\ 0 & -8.4 & 29.1 & -0.00400 & 0 & 0 \\ 0 & 0.00864 & -0.00400 & 0.0000188 & 0 & 0 \\ 0.00171 & 0 & 0 & 0 & 0.0000133 & 0.0000140 \\ -0.00912 & 0 & 0 & 0 & 0.0000140 & 0.0000500 \end{bmatrix} \quad (15)$$

Comparing $C_{pl,unbl}$ and C_{act}^{pl} it is clear that the diagonal terms c_{33}, c_{44} and c_{55} of $C_{pl,unbl}$ are about 2.5 times lower than the terms of C_{act}^{pl}. The loss of stiffness of $C_{pl,unbl}$ is mainly due to the finite stiffness in z-direction. This is because the loading of Si-leaf-springs and folded flexures of the manipulator in the z-direction, in the situation used to calculate C_{act}^{pl}, is much less. If the height of the Si-leaf-springs and folded flexures was not restricted due to fabrication limitations, the z-stiffness would be much higher. In that case the design would result in $C_{pl,unbl} \approx C_{act}^{pl}$ and each of the diagonal terms of $C_{pl,bl} \gg C_{pl,unbl}$. This would be the situation in a true exact constraint design.

The blocked stiffness of the platform couples the forces loaded onto the platform to the displacements of the platform, if the external forces $\underset{\sim}{F}_{r} = \underset{\sim}{0}$, and the actuator position is locked by a stiff mechanism. In the model the forces on the actuator nodes $\underset{\sim}{F}_{act}$ are such that $\underset{\sim}{X}_{act} = \underset{\sim}{0}$. In this case only certain parts of Eq. (3) are of

interest:

$$\begin{bmatrix} \underline{0} \\ \underline{X}_{pl} \\ \underline{X}_r \end{bmatrix} = \begin{bmatrix} S_{11} & S_{12} & \cdot \\ S_{12}^T & S_{22} & \cdot \\ S_{13}^T & S_{23}^T & \cdot \end{bmatrix} \cdot \begin{bmatrix} \underline{F}_{act} \\ \underline{F}_{pl} \\ \underline{0} \end{bmatrix} \quad (16)$$

then

$$\underline{F}_{pl} = C_{pl,bl} \cdot \underline{X}_{pl} = (-S_{12}^T S_{11}^{-1} S_{12} + S_{22})^{-1} \cdot \underline{X}_{pl} \quad \Leftarrow \underline{X}_{act} = \underline{0}; \underline{F}_r = \underline{0} \quad (17)$$

The values of $C_{pl,bl}$ are derived numerically from SPACAR and are linearized around the undeflected state. Eqs. (17) and (18) give the equation for the blocked manipulator.

$$\begin{bmatrix} F_{x,pl} \\ F_{y,pl} \\ F_{z,pl} \\ M_{x,pl} \\ M_{y,pl} \\ M_{z,pl} \end{bmatrix} = \begin{bmatrix} 822 & 0 & 0 & 0 & -0.372 & -0.773 \\ 0 & 1433 & -88.5 & 0.722 & 0 & 0 \\ 0 & -88.5 & 48.8 & -0.045 & 0 & 0 \\ 0 & 0.722 & -0.045 & 0.000392 & 0 & 0 \\ -0.372 & 0 & 0 & 0 & 0.000204 & 0.000471 \\ -0.773 & 0 & 0 & 0 & 0.000471 & 0.002493 \end{bmatrix} \begin{bmatrix} x_{pl} \\ y_{pl} \\ z_{pl} \\ rx_{pl} \\ ry_{pl} \\ rz_{pl} \end{bmatrix} \quad (18)$$

The z-stiffness is the lowest stiffness. Usually the z-stiffness is defined as $(\partial z/\partial F_z)^{-1}$, the inverse of element s_{33} of the compliance matrix. This is the experienced stiffness when a sole input force F_z is loaded onto the platform. The F_z force will not solely result in a z-displacement. In this case $(\partial z/\partial F_z)^{-1}$ = 43.3 N/m, while the pure z-displacement stiffness $\partial F_z/\partial z$ = 48.8 N/m.

The effectiveness of the clamping mechanism can be examined by comparing $C_{pl,bl}$ with $C_{pl,unbl}$. The stiffness increase in the z-direction in a blocked manipulator situation as opposed to an unblocked one is only 1.7 times. This is because the out-of-plane bending of the Si-leaf-springs is mainly responsible for the low stiffness in both cases. Therefore, clamping does not increase the stiffness in the z-direction much. The largest stiffness increase by blocking is in the rz-direction, i.e. 50 times. A true exact constraint design would show that each of the diagonal terms of $C_{pl,bl} \gg C_{pl,unbl}$.

The low stiffness of the platform in the z-direction means that small external forces cause quite a large position uncertainty. If, for an application such as micro-assembly, the position uncertainty needs to be less than 1 μm (which is still quite inaccurate), the maximum external disturbance force should be less than 50 μN in this case, which is very small.

8.6. Modal analysis

The lowest vibration mode frequencies and the accompanying vibration modes have been calculated using SPACAR and CosmosWorks. The difference between the two modeling methods is less than 5% for the lowest 10 vibration mode frequencies. The payload, a sample of 20 μm × 10 μm × 0.2 μm, does not influence the vibration mode frequencies. Fig. 12a shows the first vibration mode with unblocked actuators. The first six vibration mode frequencies with unblocked actuators ideally should resemble modes which mainly show deflection of the compliant suspension of actuators in the actuation direction. A good exact constraint design should lead to a much higher seventh vibration mode frequency (Fig. 12b). However, this is not the case with the manipulator. The relatively low vibration mode frequencies of unblocked modes 7, 8 and 9 (Fig. 12b) and blocked modes 1, 2 and 3 (Fig. 12d) are caused by the limited z-stiffness of the Si-leaf-springs. This is caused by the limited height (35 μm) to length (800 μm) ratio of the Si-leaf-springs due to DRIE fabrication. A compromise had to be made between the preferably compliant and thus low frequency unblocked actuation modes and the preferably high frequency blocked actuator modes. This is essentially a trade-off between the necessary actuator force for displacing the platform and the first vibration mode frequency. Unblocked mode 10 (Fig. 12c) and larger, and blocked modes four and larger shows internal vibration modes which have much higher frequencies as shown in Table 4. Therefore, if the out-of-plane bending stiffness of the Si-leaf-springs could be increased, the first three vibration mode frequencies of the blocked manipulator would be increased considerably. At the same time exactly 6 low frequency vibration modes for the unblocked manipulator would result, which implicates a better exact constraint design.

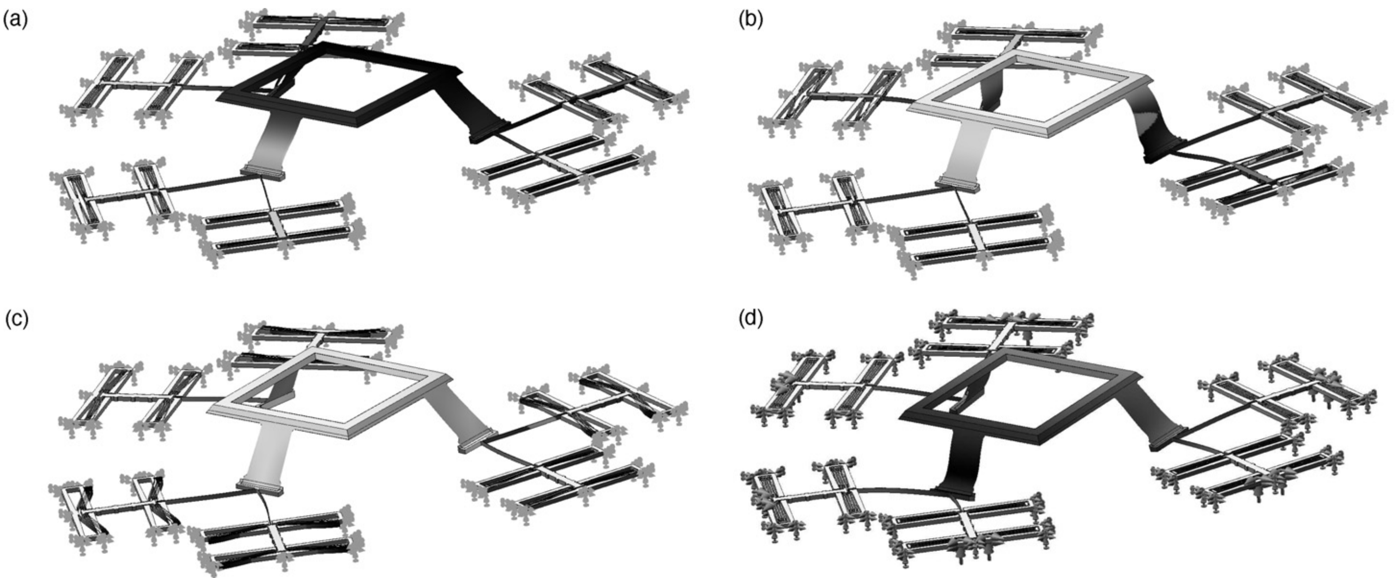

Fig. 12. Several of the lowest vibration modes of the manipulator as calculated by CosmosWorks. (a) The first vibration mode with unblocked actuators at 2.6 kHz. (b) The eighth vibration mode with unblocked actuators at 8.7 kHz. (c) The tenth vibration mode with unblocked actuators at 29.2 kHz. (d) The first vibration mode with blocked actuators at 3.8 kHz.

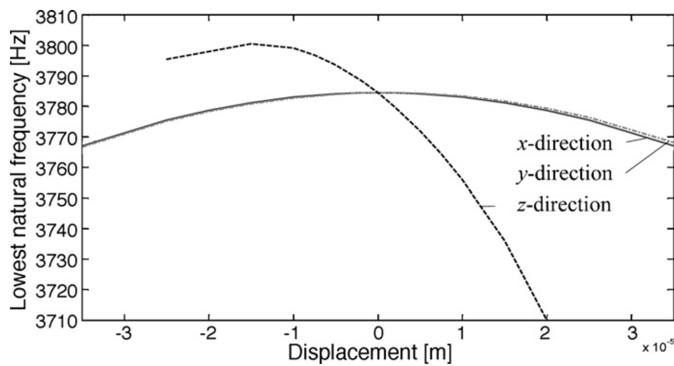

Fig. 13. The first vibration mode change with blocked actuators due to platform displacement in the x-, y-, and z-direction.

8.7. Vibration mode frequency change due to platform displacement

The stiffness of leaf-springs changes when deflected. Therefore, the vibration mode frequencies of the platform are expected to change when the platform is deflected as well. SPACAR was used to investigate this frequency shift due to a displacement in the pure x-, y- and z-translations and in the pure rx-, ry- and rz-rotation. In all cases, the actuators are blocked after initial displacement. The change of vibration mode frequency is largest for translations shown in Fig. 13.

The first vibration mode frequency with blocked actuators is a mode which mainly bends the Si-leaf-springs in the z-direction. The frequency shift of the mode is largest for a displacement in the z-direction. This shift is caused by the relatively large change in longitudinal stiffness of the slanted leaf-springs when deflected. In the x- and y-directions the slanted leaf-springs are not deflected. In-wafer-plane deflection of the Si-leaf-springs does not cause a large stiffness change in the z-direction [1]. However, the frequency shift due to platform translation is relatively small.

8.8. Stress

The stress by internal forces due to deflection of the manipulator is low. In general, this is the case if relatively low force actuators (comb-drives) are used in a compliant mechanism. The buckling load is the lowest in the x-direction on the platform, i.e. 0.21 mN. Stress caused by internal or external causes is not the failure mechanism for the manipulator, buckling is. This is the consequence of the long slender leaf-springs necessary to make the mechanism compliant enough for the low force actuators to result in the required strokes. To prevent stress concentrations due to notches, which are critical in single crystal material, all corners are rounded.

Table 4
The lowest vibration mode frequencies of the manipulator calculated by CosmosWorks.

Vibration mode frequency	Unblocked (kHz)	Blocked (kHz)
1	2.6	3.8
2	2.7	4.1
3	3.3	4.4
4	3.5	18.2
5	4.6	27.8
6	7.9	29.2
7	8.4	29.4
8	8.7	29.6
9	8.8	31.0
10	29.2	31.1

8.9. Thermal analysis

There are several sources causing thermal noise in the manipulator: the electron beam, heat producing equipment attached to the TEM column, and thermo-mechanical noise. No significant heating is caused by the electrostatic comb-drive actuators. Due to the interaction of the electrons with the sample, electrons lose about 0.02% of their energy. The electron beam heats the sample with about 20 nW. In a steady state of heat flow the maximum temperature difference between the sample and the platform will be 2.5 mK. The largest position change of the manipulator of 0.66 pm arises due to a 0.42 mK temperature increase of the slanted leaf-springs. The largest time constant of 1.9 s is small, which results in a fast adjustment of the sample and manipulator temperature to the TEM column temperature.

Thermo-mechanical noise is caused by the jiggles and jitters of matter having a finite temperature. Therefore, temperature is principally causing motion. Although a system might be in thermal equilibrium, the velocities of the molecules assume a huge range of values, but are not arbitrarily distributed. This thermal agitation of particles causes white noise and is called thermo-mechanical noise. At the micron scale the stiffness of a system can become so small that the small force fluctuation causes significant movement of the system. In AFM microscopes and in MEMS-based accelerometers this noise can be significant. The equipartition theorem [41] states that each degree of freedom which is quadratic in the Hamiltonian (such as energy storage in a spring, mass or capacitance) gets the mean energy:

$$\langle E\rangle = 0.5\,c\langle x^2\rangle = 0.5\,k_B\,T \quad (19)$$

where $\langle E\rangle$ is the mean energy, k_B is the Boltzmann constant, T is the absolute temperature, c is the spring constant related to the first vibration mode frequency and $\langle x^2\rangle$ is the variance of the position. For a blocked actuator system, a spring constant equivalent to the highest inverse compliance (the z-direction) is taken, i.e. 43.3 N/m (section 0). At 293 K, $\sqrt{\langle x^2\rangle}$ becomes 9.7 pm. Therefore, the thermo-mechanical noise has no significant influence on the positional stability of the platform. The corresponding stiffness for 1 nm thermal noise position uncertainty at 293 K is 4 mN/m, which is a very low stiffness.

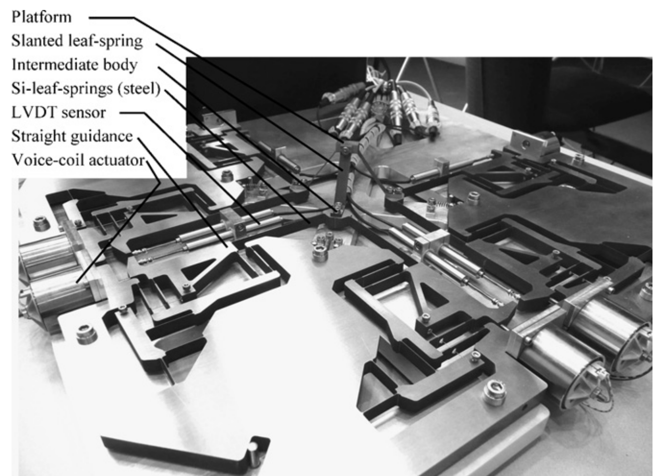

Fig. 14. The up-scaled version of the six degrees-of-freedom manipulator. The proof-of-principle is made out of Stavax a high tensile strength steel. The electrostatic actuators are replaced by voice coil actuators. LVDT sensors are included for feedback measurement.

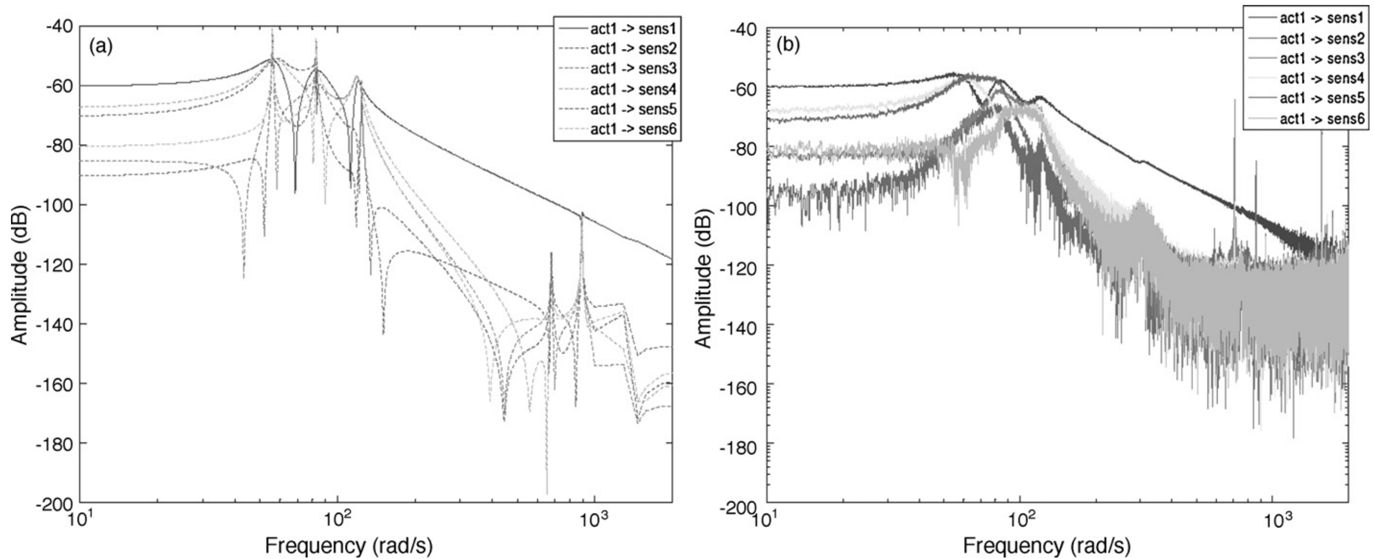

Fig. 15. (a) Modeled amplitude bode plots of force on one actuator to position of all sensors, and (b) measured amplitude bode plot of force on one actuator to position of all sensors.

9. Measurement results on scaled-up model

Since a model of this MEMS-based precision manipulator is not easy to validate, a scaled-up version, measuring 540 mm × 540 mm × 58 mm and shown in Fig. 14, has been designed and built in order to get insight into the resemblance between the model and the up-scaled version [42]. Hereby the characteristics of the MEMS-based manipulator, with the restrictions resulting from MEMS fabrication methods, have been preserved. Amongst others, these characteristics are the parallel kinematic elastic mechanism with all the actuators in one (horizontal) plane, the use of leaf-springs with a typical MEMS-based aspect ratio, and the asymmetric layout of the leaf-springs at the end-effector, which originates from the crystallographic orientation of single crystal silicon. Parts of the design, which are overconstrained, are wire spark eroded out of one piece to reduce the effects of internal stress [40] and to minimize hysteresis.

SPACAR has been used to model the transfer of force on one actuator to position of all sensors as is shown in Fig. 15a. In the measured data the damping of the back-emf of the only one connected voice coil actuator and the friction in the 6 LVDT sensors causes peaks in upper and lower direction to become smaller shown in Fig. 15b. Due to the roughly 100× larger scale and the use of steel the vibration modes frequencies are scaled as well (Table 5). Up to the 9th vibration mode, the up-scaled manipulator shows good resemblance with the SPACAR model. The 7th to 9th vibration mode frequencies have a mismatch lower than 6%, which will possibly be caused by fabrication tolerances. The distinctive peaks at 707, 861 and 1569 rad/s as well as the bump around 314 rad/s (=50 Hz) are introduced by the electronics used. Furthermore the frequencies above 1000 rad/s are difficult to distinguish, since the noise level of the sensors is higher than the displacement of the mechanism. The scaled-up model will be used for testing a control system with a combination of feedback and feed-forward. Also the position and orientation dependant dynamics which influence the controller are subject of investigation.

Table 5
The lowest vibration mode frequencies of the scaled-up manipulator modelled and experimentally acquired.

Vibration mode frequency	Model (rad/s)	Experiment (rad/s)	Relative error (%)
1	54.6	55.8	2.2
2	55.2	57.0	3.3
3	81.1	80.2	1.1
4	83.3	85.2	2.3
5	119	118	1.2
6	122	118[a]	3.4
7	624	589	5.9
8	787	753	4.5
9	836	±800[b]	4.5
10	944	–	–

[a] Frequency almost identical to mode 5, therefore difficult to measure.
[b] Frequency measured with the aid of a laser vibrometer.

10. Conclusion

A design has been presented for a six DOFs MEMS-based precision manipulator. The specifications for a precision manipulator require high frequency vibration modes combined with compliant actuation modes. The compliant actuation modes are necessary to generate sufficient displacement of +/− 10 μm by the low force MEMS actuators. Therefore, exact constraint design has been applied as much as possible. However, trade-offs had to be made between what is required from an exact constraint design point of view and what is feasible with the available fabrication processes. Therefore the height of the Si-leaf-springs is limited to 35 μm and the thickness of the leaf-springs had to be taken 3 μm. To limit the area occupied by the electrostatic actuators the mechanism needed to be compliant in the drive directions, therefore the 3 μm tick Si-leaf-springs are required to be 800 μm long. In combination with the limited height of the leaf-springs, the bending stiffness of the Si-leaf-springs in out-of-plane *z*-direction is not high compared to the compliant in-plane direction. As a consequence the six compliant actuation mode frequencies are close to the first three suspension modes with blocked actuators. At the same time the free actuator platform stiffness and the blocked actuator platform stiffness are not much different. To increase the *z*-stiffness of the platform, overconstrained design has been applied to the actuator suspension and the connection of the Si-leaf-springs to the intermediate body.

A scaled-up version of a MEMS-based six degrees-of-freedom precision manipulator has been designed, built and tested. The experiments show a great resemblance with both a FEM model and multibody model. The thermal stability for the proposed manipulator is good because of the small dimensions and the low expansion

coefficient of silicon. The overall conclusion on MEMS-based micro-mechatronic design is that precision design in MEMS is a synthesis of the fabrication process design and exact constraint design requiring trade-offs. In a MEMS-based precision design sometimes sinning against the exact constraint design principles is a necessity to obtain both a high actuation compliance and high vibration mode frequencies of the suspension modes. Future advances in fabrication technology will lead to higher leaf-springs in respect to the thickness, enabling more exactly constrained designs.

Acknowledgements

Special acknowledgement should be given to Meijaard, for his careful review of the manuscript. The authors thank J.B. Jonker, J. van Dijk and R.G.K.M. Aarts, because they enabled the extensive calculations in Spacar. M.B.P. Huijts is thanked for his precise measurements on the scaled-up model. Thanks to the collaboration with the Transducer Science and Technology group of M.C. Elwenspoek, design and fabrication of MEMS devices had been made possible. Therefore the authors like to thank G.J.M. Krijnen, and M.J. de Boer.

The research described in this article is part of the Multi Axes Micro Stage (MAMS) project and has been conducted at the chair of Mechanical Automation and Mechatronics of the department of Mechanical Engineering within the IMPACT institute at the University of Twente, Enschede, the Netherlands. The research has been financially supported by the Innovative Oriented Research Program (IOP) Precision Technology from the Dutch Ministry of Economic Affairs.

References

[1] Brouwer DM, Design principles for six DOFs MEMS-based Manipulators, PhD thesis University of Twente, Enschede, The Netherlands, ISBN 978-90-365-2510-7; 2007.
[2] Blanding DL. Exact constraint: machine design using kinematic principles; 1999, ISBN 0-7918-0085-7.
[3] Hale LC, Principles and Techniques for Designing Precision Machines, PhD thesis, Lawrence Livermore National Laboratory; February 1999.
[4] Jones RV. Instruments and experiences, papers on measurement and instrument design; 1988, ISBN 0 471 91763 X.
[5] Koster MP, Constructieprincipes voor het nauwkeurig bewegen en positioneren, Twente University Press, 2000, ISBN 903651455x.
[6] Schellekens P, Rosielle N, Vermeulen H, Vermeulen M, Wetzels S, Pril W. Design for precision: current status and trends. Cirp Ann 1998;47(2):557–86.
[7] Slocum AH. Precision machine design. Englewood Cliffs, NJ: Prentice Hall; 1992.
[8] Smith ST, Chetwynd DG, Foundations of Ultra-Precision Mechanism Design, Developments in Nanotechnology, Vol. 2, Taylor & Francis US, ISBN 2-88449-001-9; 1992.
[9] Jokiel BJ, Benavides GL, Bieg LF, Allen JJ. Planar and spatial three-degree-of-freedom micro-stages in silicon MEMS. Proc ASPE Annu Meeting 2001;25:32–5.
[10] Pister KSJ, Judy MW, Burgett SR, Rearing RS. Microfabricated hinges. Sens Actuators A 1992;33:249–56.
[11] Walraven A, Jokiel B. Failure analysis of a multi-degree-of-freedom spatial microstage. Proc SPIE 2003;4980:97–105.
[12] Yeh R, Kruglick EJJ, Pister KSJ. Surface-micromachined components for articulated microrobots. J MEMS 1996;5(1):10–6.
[13] Sarajlic E, de Boer MJ, Jansen HV, Arnal N, Puech M, Krijnen G, et al. Advanced plasma processing combined with trench isolation technology for fabrication and fast prototyping of high aspect ratio MEMS in standard silicon wafers. J Micromech Microeng 2004;14:S70–5.
[14] de Jong BR, Brouwer DM, Jansen HV, de Boer MJ, Lammertink TG, Stramigioli S, Krijnen GJM. A planar 3 DOF sample manipulator for nano-scale characterization. In: MEMS. 2006. pp. 750–753.
[15] Tas NR, Electrostatic Micro Walkers, PhD thesis, University of Twente, Enschede, The Netherlands, ISBN 90-36514355; 2000.
[16] Patrascu M, Stramigioli S, de Boer MJ, Krijnen GJM. Nanometer range closed-loop control of a microWalker for probe storage. In: Proceedings of IMECE 2007. Seattle, WA, USA: ASME; 2007.
[17] Sarajlic E, Berenschot E, Fujita H, Krijnen G, Elwenspoek M. Bidirectional electrostatic linear shuffle motor with two degrees of freedom. In: IEEE MEMS'05. 2005. pp. 391–394.
[18] Cheng W-J, DeVoe DL. Linear micromotors and spatial micromechanisms based on UVLIGA. In: IEEE MEMS'05. 2005. pp. 399–402.
[19] Fan L, Wu CW, Choquette KD, Crawford MH. Self-assembled microactuated *xyz* stages for optical scanning and alignment. In: Transducers '97. 1997. pp. 319–322.
[20] Tung Y-C, Kurabayashi K. A single-layer PDMS-on-silicon hybrid microactuator with multi-axis out-of-plane motion capabilities. Part II: Fabrication and characterization. J MEMS 2005;14(3):558–66.
[21] Sarkar N, Baur C, Stach E, Jandric Z, Stallcup R, Ellis M, et al. Modular MEMS experimental platform for transmission electron microscopy. In: IEEE MEMS. 2006. p. 146–9.
[22] Culpepper ML, Anderson G. Design of a low-cost nano-manipulator which utilizes a monolithic spatial compliant mechanism. J Prec Eng 2004;28: 469–82.
[23] Chen S-C, Culpepper ML. Design of a six-axis micro-scale nanopositioner μ-HexFlex. Prec Eng 2006;30:314–24.
[24] Ando Y. Development of three-dimensional electrostatic stages for scanning probe microscope. Sens Actuators A 2004;114:285–91.
[25] Liu X, Kim K, Sun Y. A MEMS stage for 3-axis nanopositioning. J Micromech Microeng 2007;17:1796–802.
[26] Fréchette LG, Jacobson SA, Breuer KS, Ehrich FF, Ghodssi R, Khanna R, et al. High-speed microfabricated silicon turbomachinery and fluid film bearings. J MEMS 2005;14(1):141–52.
[27] Jung IW, Krishnamoorthy U, Solgaard O. High fill-factor two-axis gimbaled tip-tilt-piston micromirror array actuated by self-aligned vertical electrostatic combdrives. J MEMS 2006;15(3):563–71.
[28] Arnold DP, Das S, Cros F, Zana I, Allen MG, Lang JH. Magnetic induction machines integrated into bulk-micromachined silicon. J MEMS 2006;15(2):406–14.
[29] Cros F, Koser H, Allen MG, Lang JH. Magnetic induction micromachine—Part II: Fabrication and testing. J MEMS 2006;15(2):427–39.
[30] Tsui K, Geisberger AA, Ellis M, Skidmore GD. Micromachined end-effector and techniques for direct MEMS assembly. JMM 2004;14:542–9.
[31] Saini R, Jandric Z, Nolan M, Mentink SAM. Microassembled MEMS minisem with carbon nanotube emitter. In: IEEE MEMS. 2006. p. 918–21.
[32] Madou MJ. Fundamentals of microfabrication; 1997, ISBN 0-8493-9451-1.
[33] Brouwer DM, de Jong BR, Soemers HMJR, Krijnen GJM. Numerical evaluation of piezo, thermo, electro-magnetic and electro-static MEMS actuators based on designs. In: EUSPEN Conference. 2006. p. 172–5.
[34] Brouwer DM, de Jong BR, de Boer MJ, Jansen HV, van Dijk J, Krijnen GJM, Soemers HMJR. MEMS-based clamp with a passive hold function for precision position retaining of micro manipulators, JMM, submitted for publication.
[35] Legtenberg R, Electrostatic actuators fabricated by surface micromachining techniques, PhD thesis, University of Twente, Enschede, the Netherlands, 1996, p. 139.
[36] Bao M, Burrer C, Esteve J, Bausells J, Marco S. Etching front control of ⟨110⟩ strips for corner compensation. Sens Actuators A 1993;37–38:727–32.
[37] Meijaard JP. Validation of flexible beam elements in dynamics programs. Nonlinear Dyn 1996;9:21–36.
[38] Timoshenko S. On the torsion of a prism, one of the cross-sections of which remains plane. Proc Lond Math Soc 1922;20:389–97.
[39] Cowper GR. The shear coefficient in Timoshenko's beam theory, Trans. ASME. J Appl Mech 1966;33:335–40.
[40] Meijaard JP, Brouwer DM, Jonker JB, Analytical and experimental investigation of a parallel leaf spring guidance, Multibody System Dynamics; accepted for publication.
[41] Gabrielson TB. Mechanical-thermal noise in micromachined acoustic and vibration sensors. IEEE Trans Electron Dev 1993;40(5). pp. 903–909.
[42] Huijts MBP, Brouwer DM, van Dijk J. Design and control of a parallel kinematic 6-DOFs precision manipulator. In: EUSPEN Conference Proceedings. 2009.